

Ground and building extraction from LiDAR data based on differential morphological profiles and locally fitted surfaces



Domen Mongus*, Niko Lukač, Borut Žalik

University of Maribor, Faculty of Electrical Engineering and Computer Science, Smetanova 17, SI-2000 Maribor, Slovenia

ARTICLE INFO

Article history:

Available online 10 January 2014

Keywords:

LiDAR
Ground extraction
Buildings detection
Mathematical morphology
DMP
LoFS

ABSTRACT

This paper proposes a new framework for ground extraction and building detection in LiDAR data. The proposed approach constructs the connectivity of a grid over the LiDAR point-cloud in order to perform multi-scale data decomposition. This is realised by forming a top-hat scale-space using differential morphological profiles (DMPs) on points' residuals from the approximated surface. The geometric attributes of the contained features are estimated by mapping characteristic values from DMPs. Ground definition is achieved by using features' geometry, whilst their surface and regional attributes are additionally considered for building detection. A new algorithm for local fitting surfaces (LoFS) is proposed for extracting planar points. Finally, transitions between planar ground and non-ground regions are observed in order to separate regions of similar geometrical and surface properties but different contexts (i.e. bridges and buildings). The methods were evaluated using ISPRS benchmark datasets and show superior results in comparison to the current state-of-the-art.

© 2013 International Society for Photogrammetry and Remote Sensing, Inc. (ISPRS) Published by Elsevier B.V. All rights reserved.

1. Introduction

Light Detection and Ranging (LiDAR) technology has become the focus of research over recent years, as increasingly more attention is being paid to Earth observations. Since airborne LiDAR systems provide an efficient solution for rapid high-resolution 3D mapping of the Earth's surface, the main research focus is currently on information extraction from LiDAR data. The extraction of the ground for the generation of a digital terrain model (DTM) is a key-step of this process. It can be interpreted as a background when considering the detection of above-the-surface objects such as buildings. Namely, numerous methods perform so-called normalisation by subtracting DTM from the LiDAR data (Lohmann et al., 2000).

According to the literature (Sithole and Vosselman, 2004; Liu, 2008), ground filtering methods can be described as slope-based (Vosselman, 2000; Sithole, 2001; Shan and Sampath, 2005; Wang and Tseng, 2010), linear prediction-based (Brovell et al., 2004; Kraus and Pfeifer, 1998; Pfeifer et al., 1999; Lee and Younan, 2003), and methods based on mathematical morphology (Zhang et al., 2003; Zhang and Whitman, 2005; Chen et al., 2007; Mongus and Žalik, 2012, in press; Pingel et al., 2013). The slope-based

methods filter non-ground points based on the assumption that their gradients are distinctively different from the gradients of the ground points. Consequently, they are highly-suitable for ground extraction on flat areas but their accuracies decrease with increasingly steeper slopes (Liu, 2008). The linear prediction-based methods use a rough surface approximation in order to minimise the influence of terrain undulation where filtering is achieved by thresholding points' residuals from the approximated surfaces. Consequently, they have difficulties in filtering small objects and detecting terrain details such as cliffs or sharp ridges (Sithole and Vosselman, 2004; Liu, 2008). Although morphological methods are generally more robust to these conditions, the choice of a structuring element plays an important role when considering their accuracies. A small structuring element can efficiently filter out small objects, however larger objects (e.g. buildings) remain preserved. Although a larger structuring element provides a solution to this problem, on the other hand it flattens terrain details such as mountains' peaks, ridges, and cliffs. Several advances in ground filtering have recently been made by so-called hierarchical morphological approaches relying on gradually increasing structuring elements. Zhang et al. (2003) proposed comparing elevation differences before and after applying morphological openings at increasing scales. Chen et al. (2007) extended this approach on areas with changing inclines by defining a set of tunable parameters describing terrain topography. Mongus and Žalik (2012) proposed a parameter-free approach that was recently upgraded by Chen

* Corresponding author. Tel.: +386 2 220 7408; fax: +386 2 220 7272.

E-mail address: domen.mongus@uni-mb.si (D. Mongus).

URL: <http://gemma.uni-mb.si> (D. Mongus).

et al. (2013) where terrain undulations are approximated by surface interpolation and a hierarchical morphological approach is applied to points' residuals from the surface. Pingel et al. (2013) advanced a simple morphological filter (SMRF) by thresholding slopes defined by the ratios between elevation differences and opening sizes. Mongus and Žalik (in press) on the other hand proposed a computationally efficient method based on multi-scale decomposition using connected operators. In most cases ground extraction is considered as a separate problem, where object detection is performed independently on the non-ground points.

Buildings are particularly important and extensively studied amongst the numerous features contained in the LiDAR data. According to our study, the approaches towards building detection can be classified as fitting-based methods, morphological methods, and supervised learning approaches. The fitting-based methods are the more popular as they allow a clear integration of pre-existing knowledge regarding buildings' shapes (Rottensteiner and Briese, 2002; You et al., 2003). As not all the possible shapes of buildings can be modelled in advance the plane-fitting approaches provide more general solutions (Alharthy and Bethel, 2002; Rottensteiner, 2003; Zhou et al., 2004; Ruijin, 2005; Verma et al., 2006; Zhang et al., 2006; Tarsha-Kurdi et al., 2007; Neidhart and Sester, 2008; Dorninger and Pfeifer, 2008; Sampath and Shan, 2010; Kim and Shan, 2011). Usually by minimising the mean-square error, these approaches perform a surface analysis in order to identify planar sets of points by which buildings can be distinguished from natural features such as vegetation. The state-of-the-art algorithms such as Random Sample Consensus (RANSAC) (Verma et al., 2006) and Hough-transform (Tarsha-Kurdi et al., 2007) can be considered when transforming a building detection problem to a surface-fitting problem. Hough-transform is computationally inefficient and sensitive to the fitting parameters. Moreover, the voting procedure forming the accumulator space requires additional filtering in order to obtain an exact surface definition. Although computationally more efficient, RANSAC often detects undesirable planes within the vegetation areas due to random sampling. Tarsha-Kurdi et al. (2007) proposed a modified version of RANSAC that considers buildings' roofs' geometries. A more recent method by Kim and Shan (2011) uses the level-set method for plane-fitting and consequently the detection of buildings. Realistically, fitting approaches are, in general, computationally demanding as they are iterative. Moreover, additional geometrical attributes (e.g. sizes and shapes) need to be considered for achieving sufficient accuracy.

Over recent years several morphological methods have been proposed for building detection that rely more on their geometrical properties. Zhang et al. (2006) proposed a straightforward building detection based on the observation that vegetation is filtered on significantly smaller filtering scales. Vu et al. (2009) considered LiDAR data within a multi-scale morphological space where clustering was adopted for building detection. Area and shape compactness attributes were considered for building detection by Meng et al. (2009), whilst Chen et al. (2012) improved progressive morphological filtering by additionally applying a region growing algorithm based on RANSAC. Cheng et al. (2013) have improved the reverse iterative mathematical morphological (RIMM) approach proposed by Zhang et al. (2003). This method overcomes the constant slope constraint by using a dynamic threshold function applied on height differences introduced by progressive filtering. Mongus et al. (2013) solve the problem of buildings with considerably different shapes and sizes by applying differential attribute profiles. However, the proposed method has difficulties in distinguishing between buildings and objects of similar geometry (e.g. bridges or miss-classified terrain plateaus). Although this issue has already been exposed by several authors (e.g. in Forlani et al. (2006) and Rottensteiner et al. (2007)), it has not yet been sufficiently dealt-with. Partial solutions may, however, be found

when considering bridges within the context of road extraction, e.g. Clode et al. (2005) and Evans (2008).

Several methods have also been proposed based on supervised learning, a well known paradigm in pattern-recognition. In this case, an already labelled LiDAR point-cloud serves as a training dataset for artificial neural networks (Priestnall et al., 2000), expected maximisation (Charaniya et al., 2004), Bayes classifier (Wang et al., 2006), support vector machines (Mallet et al., 2008), self-organising maps (Salah et al., 2009), and decision trees (Hermosilla et al., 2011). These approaches require preprocessing steps in order to extract geometrical (e.g. slope, orientation), topological (e.g. number of k-nearest neighbours) or textural (i.e. wavelet transform) features from points. Although these methods have proven to be accurate, their performances highly depend on the training datasets and the properties of the considered features. They are also computationally less efficient (Dietterich, 2002). Additional improvements in building detection can be achieved by fusing LiDAR data with numerous types of aerial images. This can significantly contribute to the accuracies of the methods by providing supplementary information beyond the scope of LiDAR systems (e.g. surface reflectance in multiple electromagnetic bands). Nevertheless, this data may not always be available and accurate processing of LiDAR data alone is still required.

This paper proposes two new algorithms for feature detection within LiDAR data joined within a common framework, which is schematically presented in Fig. 1. Firstly, a new mapping schema for ground extraction is derived by combining surface approximation with multi-scale data decomposition using differential morphological profiles (DMPs). Estimated geometrical properties are further considered for building detection where supplementary surface analysis is achieved by a new algorithm for the estimation of locally fitted surfaces (LoFS). Finally, regional analysis is performed by inspecting the transitions between ground and non-ground regions in order to incorporate contextual information that allows for distinguishing between objects sharing similar geometrical and surface properties, e.g. buildings and bridges.

The key novelties, proposed in this paper, can be exposed as follows:

- A combination of DMPs with surface approximation for reducing the influence of large terrain undulations is proposed. It provides a mathematically correct concept of analysing the geometric properties of the contained objects.
- By supplementing those geometrical attributes used for ground filtering with surface and regional attributes, a common framework is introduced for both problems. As confirmed by the results, the accuracies of both are significantly correlated.
- The concept of LoFS is introduced and its efficiency for surface analysis is shown in comparison with the related methods.
- Differentiating between buildings and objects that share the same geometric and surface attributes (e.g. bridges) is efficiently achieved by regional attachment analysis.

The rest of the paper is organised as follows: a new ground filtering approach is proposed in Section 2. Section 3 introduces a new method for building detection. The results of both methods are presented in Section 4. Section 5 concludes the paper.

2. Generating a digital terrain model

A new method for the generation of a digital terrain model (DTM) from LiDAR data is proposed in this section. The robustness of the method against terrain undulations is achieved by estimating a rough surface approximation where multi-scale decomposition based on differential morphological profiles (DMPs) allows

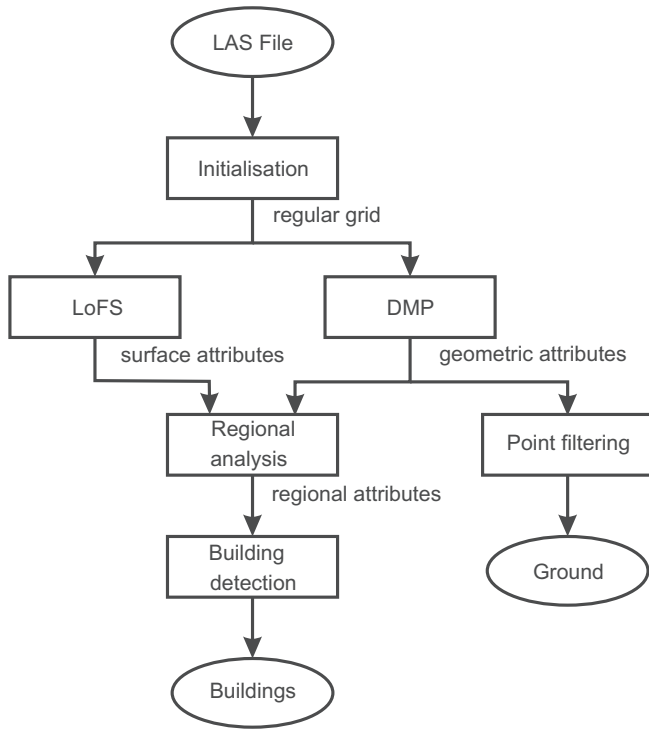


Fig. 1. Framework of the proposed method for ground and building extraction, where regular grid is constructed over the input LiDAR points during the initialisation step. DMPs are used for the estimation of geometric attributes based on which ground points are filtered. Additionally, surface attributes (obtained by LoFS) are used and region analysis is performed in order to obtain a set of building points.

for the filtering objects of different sizes and shapes. The outline of the method is given over the following three steps:

- **Initialisation** constructs a regular grid over the input LiDAR point-cloud.
- **Construction of DMP** is performed on points' residuals from the approximated ground.
- **Point-filtering** is done by thresholding maximal responses registered in DMP and the generated DTM is used for labelling LiDAR point-cloud.

In a certain sense, this method could be considered as a conceptual extension of Mongus and Žalik (2012, in press), by combining surface approximation with multi-scale decomposition. Nevertheless, Mongus and Žalik (2012) used a bottom-up approach where surface interpolation is performed at each step without considering the grid's decomposition. On the other hand, Mongus and Žalik (in press) use data decomposition alone. In their work, differential attribute profiles and Θ -mapping for the estimation of standard deviations are used, whilst the proposed method is based on DMPs. Each of the steps is explained in the continuation.

2.1. Initialisation

During initialisation, connectivity between points is established by the construction of a grid $g: E \rightarrow \mathbb{R}$ over the input LiDAR point-cloud $L = \{l_i\}$ that occupies the space E (i.e. E is determined by the bounding-box of L), where $p \in E$ is a grid-point. Recapitulated from Mongus et al. (2013), the construction of g is done over the following three steps:

- R_g defines the resolution of g , estimated according to the LiDAR data density D_L as $R_g = 1.0/D_L$,

- $g[p]$ is the value of g at p given by the lowest point contained within the corresponding grid-cells, and
- p^* denotes an undefined grid-point (i.e. $g[p^*] = \text{UNDEF}$) obtained when no points are contained within the corresponding grid-cell. In this case, $g[p^*]$ is estimated by inverse distance weighting. According to Chaplot et al. (2006), accurate spatial interpolation is achieved by

$$g[p_n^*] = \frac{\sum_{p_n \in W_{p_n^*}} g[p_n] d_{p_n}^{-r}}{\sum_{p_n \in W_{p_n^*}} d_{p_n}^{-r}}, \quad (1)$$

where p_n is a point from the neighbourhood $W_{p_n^*}$ of p_n^* that contains no less than the three nearest points (i.e. $|W_{p_n^*}| \geq r$), d_{p_n} is the Euclidean distance between p_n^* and p_n , and $r = 2$ is the power parameter that defines the smoothness of the interpolation. In continuation, interpolated values and values obtained from LiDAR data are treated in the same way.

Note that only a topology of a grid is established in this way and the actual processing is performed with the floating-point values. After g is constructed, low outliers (points lying below the ground as a consequence of multi-path errors or errors in the laser range finder) are removed as proposed in Mongus and Žalik (2012).

2.2. Decomposition of grid and feature mapping

This section explains the multi-scale grid decomposition for mapping the characteristic values of features contained in g for efficient DTM generation (as well as the building-extraction proposed in Section 3). Note that in contrast to the related methods where data filtering is straightforwardly applied (e.g. the SMRF algorithm explained in Pingel et al. (2013)), this step increases the accuracy of the filtering by mapping the characteristics of the contained features from the top-hat scale-space constructed over the textural part of g . For this purpose, the decomposition of g into a low g^l and a high g^h frequency bands is performed first. This is achieved by convolving g with a Gaussian kernel G that is large enough to remove all the contained non-ground features (the size of the contained objects is discussed in the continuation). Formally, g^l and g^h are given by

$$g^l = g * G, \quad (2)$$

$$g^h = g - g^l, \quad (3)$$

where $*$ is convolution. By containing low-frequency terrain undulations, g^l provides a rough approximation of the ground surface. Ground details as well as non-ground features are contained in g^h . Further processing is therefore performed only on g^h .

Let $\gamma_{w_s}(g^h)$ be a morphological opening acting on g^h , where w_s is a disc-shaped structuring element of size s (note that only disc-shaped structuring elements and windows are considered in this paper). The multi-scale decomposition of g^h is achieved by using the granulometry of morphological openings i.e. a series of morphological filters that remove the content of g^h in a progressive manner (Maragos, 1989). For this purpose an ordered set of filtering scales $\mathbf{s} = \{s_i\}$ is defined as

$$\mathbf{s} = \{0, 1, 2, \dots, S\}, \quad (4)$$

where S corresponds to the size of the largest contained object. A top-hat scale-space $\Delta(g^h)$, known as DMPs (Pesaresi and Benediktsson, 2001), is given by

$$\Delta(g^h) = \{\gamma_{w_{s_{i-1}}}(g^h) - \gamma_{w_{s_i}}(g^h)\}, \quad (5)$$

where $i \in [1, I]$ and $I = \text{cardinality}(\mathbf{s}) - 1$. $\Delta(g^h)$ is therefore a decomposition of g^h , where $\Delta(g^h)[p]$ is an I -long response-vector (a vector containing the height differences associated with each $\gamma_{w_{s_i}}$)

assigned to a particular point p (see Fig. 2). Note that DMPs are defined based on morphological opening in contrast to Pesaresi and Benediktsson (2001), where opening by reconstruction is considered.

In our case, three important characteristics of the features are mapped from $\Delta(g^1)$:

- g' is a function registering the largest responses from $\Delta(g^1)$ obtained at each point p ,
- g^* is a function describing the smallest scales at which the largest responses are registered, and
- g^+ is a function containing the sum of the responses registered before and including the largest response (note that g^+ is not used for DTM generation but for the building detection considered in Section 3).

Let \vee be a supremum (i.e. the upper bound) and \wedge an infimum (i.e. the lower bound). Formal definition of the function $\Theta_{w_s}(g^1)$ that estimates g' , g^* , and g^+ at point p is given as

$$\begin{aligned} \Theta_{w_s}(g^1) : g^1 &\rightarrow (g', g^*, g^+), \\ g'[p] &= \bigvee_{i \in [1, I]} \Delta(g^1)[p][i], \\ g^*[p] &= \bigwedge_{i \in [1, I]} s_i | \Delta(g^1)[p][i] = g'[p], \\ g^+[p] &= \sum_{i \leq g^*[p]} \Delta(g^1)[p][i]. \end{aligned} \quad (6)$$

In brief, g' describes the height differences of features from their surroundings, g^* provides an estimation of their sizes (in terms of their widths), and g^+ is an estimation of their heights.

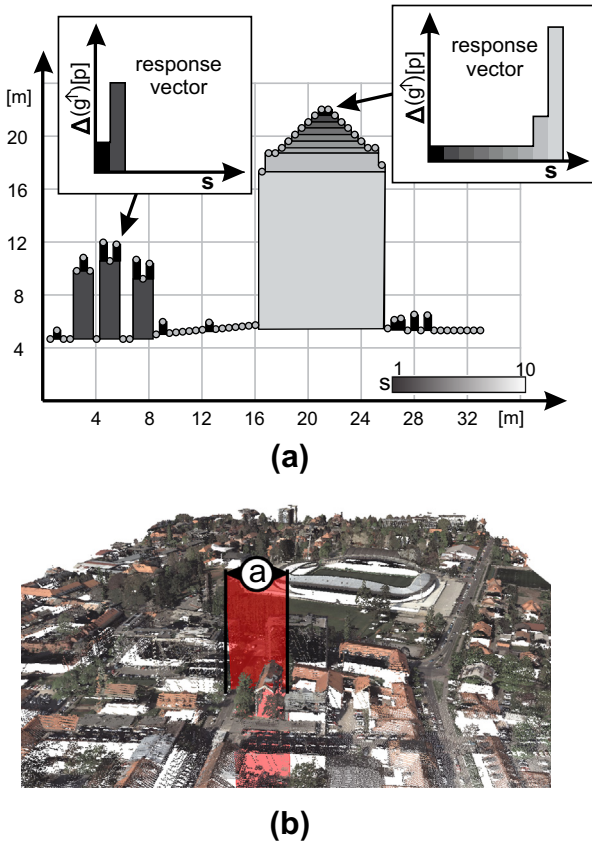


Fig. 2. Decomposition of a grid achieved by (a) progressive filtering of g^1 at increasing scales s , where a response vector $\Delta(g^1)[p]$ is assigned to each grid-point, estimated from (b) the input LiDAR point-cloud.

2.3. Point-filtering

By considering the ground as a smooth continuous surface (Haugerud and Harding, 2001), an obvious solution for DTM generation is to threshold g' in order to identify and remove those features that do not fulfil this assumption. However, low non-ground objects may still produce mild responses, whilst those responses obtained in the cases of mountain peaks and sharp ridges may be strong. Thus, a threshold function should additionally consider the sizes of the features mapped by g^* . Namely, when considering relatively small features mild responses may be enough to recognise them as non-ground and larger threshold values should be applied when considering larger features. This observation leads to a linear definition of a threshold function $T(g^*)$, given at p as

$$T(g^*)[p] = kg^*[p] + n. \quad (7)$$

The set of ground points S_G is then obtained by

$$S_G = \{p | g'[p] < T(g^*)[p]\}. \quad (8)$$

DTM construction is finalised when non-ground points $S_{NG} = E \setminus S_G$ are interpolated using Eq. (1).

In the final step, the labelling of input LiDAR points is performed according to their height differences from DTM. Since the construction of g is achieved by selecting the lowest points contained within the grid-cells, it can be concluded that the great majority of ground-points lie above the ground. It can also be expected that their height differences from DTM are in correlation with the slope gradient. Consequently, the proposed threshold function is based on the external morphological gradient ∂DTM , where $\partial DTM = \delta_{w_1}(DTM) - DTM$ and $\delta_{w_1}(DTM)$ is a morphological dilation using the structuring element of the smallest size i.e. 3×3 . A set of ground-points $L_G \subset L$ from the input LiDAR point-cloud L is obtained by

$$L_G = \{l_i | d_h(l_i) < \partial DTM[p] + b\}, \quad (9)$$

where $d_h(l_i)$ is the absolute height difference between DTM and an input LiDAR point $l_i \in L$, and b is a user-defined constant. In total four user-defined parameters are used, where the generation of DTM is achieved by defining the maximal size of the contained non-ground feature S (namely its width). k and n describe the correlation between the features' sizes and residuals. Constant b is then used only for point labelling and defines the maximal height-difference between ground-points and DTM.

3. Building extraction

A set of non-ground points S_{NG} , obtained during DTM generation, is segmented during this step into sets of building and non-building points. The buildings are considered as large above-the-ground objects with planar surfaces. The proposed method detects buildings by considering three types of attributes:

- **geometric attributes** describing the widths and heights of features,
- **surface attributes** describing the surface curvatures at each point, and
- **regional attributes** describing areas of non-ground regions and their transitions to ground regions.

Note that the geometric attributes are obtained by Θ_{w_s} as defined in Eq. (6), whilst the estimations of surface and regional attributes are described in the continuation.

3.1. Locally-fitted surfaces

This section introduces the concept of Locally Fitted Surfaces (LoFS), proposed for the identification of points forming surfaces with low curvature (i.e. planes). When considering the related methods described in Section 1 some general properties that are desirable when applying surface fitting to LiDAR data are exposed first:

- **Locality** requires from points forming the same surface to be near enough to consider them as points belonging to the same feature.
- **Resistance to noise** describes the method's ability to bridge the obstacles (e.g. trees covering the rooftop or points within the building as a consequence of low outliers or due to rooftop transparency) and link points lying on the same surface although they might be disconnected.
- **Computational efficiency** should be ensured (e.g. by avoiding iterative approaches) when processing large data sets.

In order to satisfy these requirements a set of surfaces is firstly estimated by fitting them to the neighbourhoods of given points (each point is, thus, linked with a single surface). Note that when the neighbourhood of a given point does not lie on the same surface (e.g. near the edge of a building or an obstacle on its surface) such a fitting results in a large fitting-error. When this is the case, a surface to which a given point fits better should exist. In particular, this surface should be linked with one of the points lying in the neighbourhood of a given point on the opposite side of the edge or an obstacle. A neighbourhood of each point is therefore inspected in order to link it with a surface to which it fits best.

We denoted by $w_F^p \subset E$ and $w_L^p \subset E$ the fitting and the linking windows translated to p where F and L define their extents, respectively (in our case $F \leq L$). An arbitrary polynomial function given in implicit form (i.e. $\Pi[p] = 0$) can then be fitted to w_F^p by minimising the square errors. Since the least-square fitting is well-known, it is not discussed here. An in-depth study of the least-squares is provided in Bevington and Robinson (2002) and estimation of the best-fitted planes (used in the proposed method) is explained in Appendix A. A set of fitted surfaces is denoted as $\Pi_{w_F}^g$ and $\varepsilon_{w_F}^g$ is a function of the corresponding sum of square-errors. The relationship between $\Pi_{w_F}^g(p)$ and $\varepsilon_{w_F}^g[p]$ at p is given as

$$\varepsilon_{w_F}^g[p] = \sum_{q \in w_F^p} \Pi_{w_F}^g(q)[p]^2. \quad (10)$$

LoFS-transformation is then described as a mapping function $LoFS(g, w_F, w_L) : g \rightarrow (\Pi(g), \varepsilon(g))$ given at p by

$$\begin{aligned} \varepsilon(g)[p] &= \bigwedge \varepsilon_{w_F}^g[q] + \Pi_{w_F}^g(q)[p]^2 | q \in w_L^p, \\ \Pi(g)[p] &= \Pi_{w_F}^g(q) | \varepsilon(g)[p] = \varepsilon_{w_F}^g[q] + \Pi_{w_F}^g(q)[p]^2, \end{aligned} \quad (11)$$

where $\Pi(g)$, called a surface-function, provides implicit equations of the fitted surfaces and $\varepsilon(g)$ is an error-function describing the fitting quality. When considering the fixed values of F and L it can be shown that a constant number of operations per point is needed for LoFS estimation, leading to a linear computational complexity regarding the number of grid points.

In order to better illustrate the concept of LoFS transformation, consider the examples from Fig. 3a, where a cross-section of a building's surface can be seen corrupted by several obstacles. $\Pi_{w_3}^g$ is estimated during the fitting step, as shown in Fig. 3b. Note that $F = 3$, thus each surface is fitted to a given point by also considering its left and right neighbours. Each point is linked with a corresponding surface, as shown in the examples from Fig. 3c.

The linking step is then performed with $L = 5$. Thus, the darkened point from the first example is linked with the surface corresponding to the second point on its right. By the same principle, both darkened points from the second examples are linked with the surfaces of their neighbours (surfaces not linked by any of the points are removed). However, in the third example the darkened point is not linked with the dashed surface as it corresponds to a point outside of the linking-window. The obtained building's surface (shown in Fig. 3e) is, therefore, only partially reconstructed. Using a large L would obviously improve the results in this case.

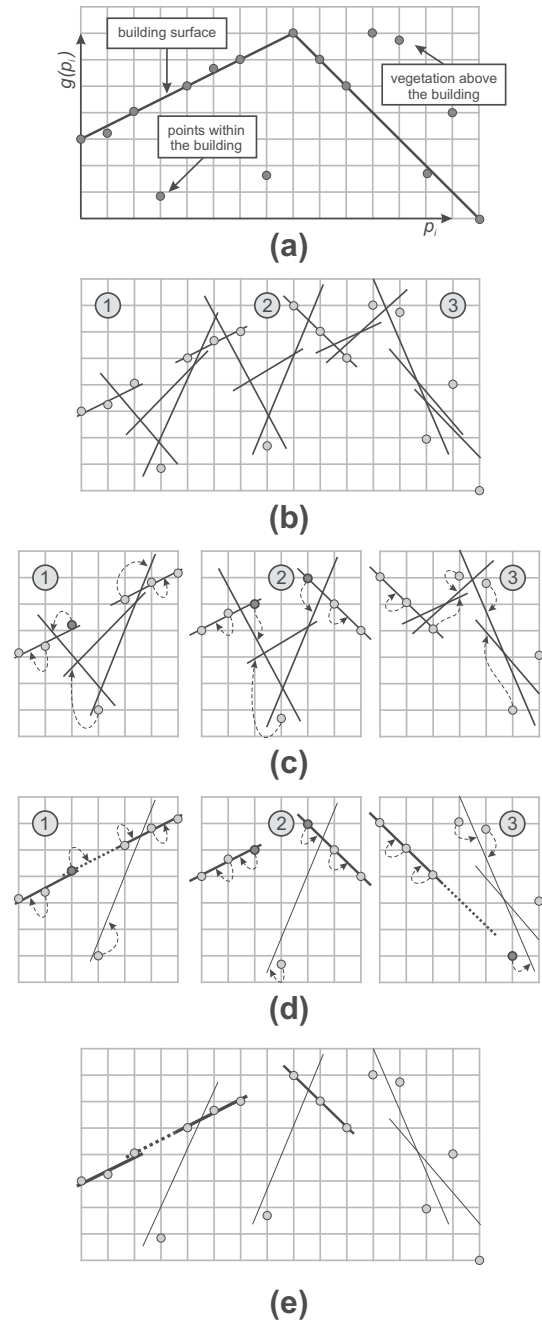


Fig. 3. Estimation of LoFS with $F = 3$ and $L = 5$ in the case of (a) a noisy building surface. Firstly, (b) a set of best-fitting surfaces $\Pi_{w_F}^g$ is obtained, and (c) the surfaces are linked with the corresponding points (three examples are shown). Then (d) the neighbourhood of each point is searched in order to link it with a surface to which it fits best in (e) the final set of surfaces $\Pi(g)$ (thickened surfaces have small fitting errors $\varepsilon(g)$).

3.2. Building detection

The proposed method constructs the following three sets of points for regional analysis by considering the geometrical and surface properties estimated by Θ and $LoFS$ (see Eqs. (6)–(11)):

- S^p is a set of points thresholded according to the error function ε associated with $LoFS$. Since plane-fitting is used in our case (description of the best-fitting plane is given in Appendix A), S^p is referred to as a set of planar-points. Formally, S^p is obtained by

$$S^p = \{p | \varepsilon(g)[p] \leq T^p\}, \quad (12)$$

where $p \in E$ and T^p is a user-defined threshold that corresponds to the maximal curvature (or roughness) of the buildings' surfaces.

- S_G^p is a set of planar ground points given by

$$S_G^p = S_G \cap S^p, \quad (13)$$

where S_G is a set of ground points obtained by Eq. (8), and

- S_{NG}^p is a set of planar non-ground points defined by

$$S_{NG}^p = S_{NG} \cap S^p. \quad (14)$$

Although buildings are considered to be non-ground features with planar surfaces, not all the points from S_{NG}^p correspond to the actual buildings as planar regions may describe various objects (e.g. walls, cars, or bridges). A further condition complementing Eq. (14) is that $g^+[p] \geq t^w$ and $g^+[p] \geq t^h$, where t^w and t^h are user-defined width and height thresholds.

S_{NG}^p is therefore a thresholded set of points satisfying the geometrical and surface conditions defined for buildings. The final step considers the connected components of S_{NG}^p (i.e. connected subsets of points or regions contained in S_{NG}^p). The rationale behind applying a regional-based approach is that the connected components correspond to building candidate regions and, when observing their neighbourhoods, contextual information can be obtained. One important case is when considering the differences between buildings and bridges that may own similar geometrical and surface properties. However, bridges are attached to the ground from at least two different sides, whilst one attachment at most is expected when considering buildings. In this context a regional-attachment analysis is performed first. Let $C_k \subset S_{NG}^p$ be a connected component from S_{NG}^p , where $k \in [1, K]$ is its index. The attachment of C_k to the ground can be described as the area where C_k meets a ground region from S_G^p on a planar region from S^p . Formally, a set of attaching points $S_{C_k}^A$ corresponding to a particular C_k is obtained by

$$S_{C_k}^A = (\delta_{w_1}(S_G^p) \cap S^p) \cap C_k, \quad (15)$$

where δ is a morphological dilation. $S_{C_k}^A$ may contain several connected components, each corresponding to different attachments. Since buildings may be attached to the ground at one side, the largest attachment (i.e. the largest connected component from $S_{C_k}^A$) is not in our interests. However, we can sufficiently preserve buildings and remove bridges by filtering all C_k with the area of the second-larger attachment above some predefined threshold. In order to formalise this observation, let us denote an attribute function that estimates the second larger attachment of C_k as $A_{(2)}(S_{C_k}^A)$. In accordance with the theory of the connected operators (Salember and Wilkinson, 2009), the top-hat of an attribute opening is applied in order to obtain a set of building candidates B_c as

$$B_c = S_{NG}^p - \gamma_{t^s}^{A_{(2)}}(S_{NG}^p), \quad (16)$$

where $\gamma_{t^s}^{A_{(2)}}(S_{NG}^p) = \{C_k \in S_{NG}^p | A_{(2)}(S_{C_k}^A) \geq t^s\}$ is an attribute opening that removes all the connected components C_k with a second-larger

attachment smaller than the threshold t^s . Finally, area opening and closing are performed in order to remove small regions that might be related to noise and fill possible holes within the building-regions. By denoting area function as $A(C_k)$ and area closing as $\phi_{t^A}^A$, the final set of building regions B is obtained by

$$B = \gamma_{t^A}^A(\phi_{t^A}^A(B_c)), \quad (17)$$

where t^A corresponds to the area of the smallest-building. Together with t^w and t^h defining the minimal widths and heights, t^r defining the maximal second larger attachment, and t^p corresponding to surface roughness, five user-defined parameters are needed to obtain a set of building regions. The proposed method, moreover, allows for straightforward point-labelling. By considering the surface function associated with $LoFS$, the distance from the building surface can be estimated for each input point $l_i \in L$ and t^p can be used once more for thresholding them. Formally, a set of building LiDAR points L_B is obtained by

$$L_B = \left\{ l_i | \bigcap_{q \in w_F^i} \Pi_{w_F}^g(q)[l_i]^2 < t^p \right\}, \quad (18)$$

where w_F^i defines the neighbourhood of l_i .

4. Results

The proposed methods were evaluated on two different benchmark test-sets, the first was designed to test ground extraction and the second to test building detection. Since the accuracy of building detection is strongly subject to the accurate extraction of ground (and consequentially non-ground) points, the proposed method for ground filtering was considered first.

4.1. Evaluation of ground-filtering method

The first tested dataset was a benchmark provided by the International Society for Photogrammetry and Remote Sensing (ISPRS) Commission III/WG2 (<http://www.commission3.isprs.org/wg2/>). It consists of fifteen samples with point-spacing between 1 m and 1.5 m in the urban (samples *samp11* to *samp42* in Table 1) and between 2 m and 3.5 m in the rural areas (samples *samp51* to *samp71* in Table 1). Each sample contains particular features, where the filtering algorithms are likely to fail (see Sithole and Vosselman (2004) for details). In order to achieve optimal performance, a different set of parameters was used for each sample dataset and the obtained results were compared with the improved SMRF algorithm by Pingel et al. (2013) and the improved Mongus and Žalik (2012) as proposed by Chen et al. (2013). The accuracy of the proposed ground-filtering method (together with the parameters used to achieve them) is shown in Table 1, where Type I error gives the percentage of rejected ground points and Type II error is the percentage of accepted non-ground points. The implementation used in this evaluation is available at <http://gemma.uni-mb.si/gLiDAR>. The tests were performed on Intel® Core™ i7 CPU with 8GB of main memory and the achieved execution times were in all the cases below 0.5 s (note that these test examples contain less than 55,000 points). However, the execution time depends mainly on the value S as the estimation of DMPs is computationally the most demanding. Using current implementation, the execution time could roughly be estimated at 8 s per million points.

The results from Table 1 show the efficiency of the proposed method. It outperformed Chen et al. (2013) in all cases and significantly reduced the average Total error as well as the standard deviation of the results. The proposed method was also more

Table 1

Comparison of the proposed method for ground-filtering with [Chen et al. \(2013\)](#) and SMRF on ISPRS benchmark datasets. The minimal total errors achieved in particular cases are highlighted.

	Used parameter				The proposed method			SMRF by Pingel et al. (2013)			Chen et al. (2013)		
	S (m)	k	n	b	Total error (%)	Type I error (%)	Type II error (%)	Total error (%)	Type I error (%)	Type II error (%)	Total error (%)	Type I error (%)	Type II error (%)
<i>samp11</i>	30	0.20	0.30	0.20	7.50	6.17	9.28	8.28	7.88	8.81	13.01	19.25	4.62
<i>samp12</i>	30	0.10	0.15	0.35	2.55	2.28	2.84	2.92	2.57	3.30	3.38	3.99	2.75
<i>samp21</i>	40	0.07	0.20	0.50	1.23	0.37	4.28	1.10	0.26	4.07	1.34	0.75	3.41
<i>samp22</i>	40	0.10	0.30	0.25	2.83	1.79	5.12	3.35	2.57	5.07	4.67	2.65	9.11
<i>samp23</i>	24	0.30	0.25	0.25	4.34	3.26	5.55	4.61	3.21	6.17	5.24	4.45	6.11
<i>samp24</i>	20	0.25	0.15	0.25	3.58	2.34	6.85	3.52	2.25	6.90	6.29	5.54	8.26
<i>samp31</i>	40	0.05	0.15	0.25	0.97	0.31	1.74	0.91	0.39	1.52	1.11	0.55	1.77
<i>samp41</i>	50	0.25	0.50	0.45	3.18	2.14	4.21	5.91	3.64	8.17	5.58	9.07	2.11
<i>samp42</i>	130	0.01	0.85	0.20	1.35	0.58	1.67	1.48	0.27	1.98	1.72	4.70	0.48
<i>samp51</i>	30	0.08	0.30	0.10	2.73	0.72	9.94	1.43	0.59	4.44	1.64	0.73	4.88
<i>samp52</i>	30	1.00	0.30	0.25	3.11	1.26	18.88	3.82	3.09	10.08	4.18	3.06	13.76
<i>samp53</i>	6	0.10	1.00	0.55	2.19	0.67	38.44	2.43	1.18	31.97	7.29	7.15	10.51
<i>samp54</i>	30	0.25	0.05	0.10	2.16	1.76	2.51	2.27	2.51	2.05	3.09	3.44	2.79
<i>samp61</i>	6	0.20	0.60	0.25	0.96	0.20	22.39	0.86	0.51	10.70	1.81	1.70	4.98
<i>samp71</i>	20	0.40	0.50	0.25	2.49	0.78	15.88	1.65	0.99	6.84	1.33	0.35	8.98
Average					2.74	1.64	9.97	2.97	2.13	4.47	4.11	4.49	5.63
Standard deviation					1.64	1.55	10.15	2.07	1.99	7.37	3.17	4.80	3.76

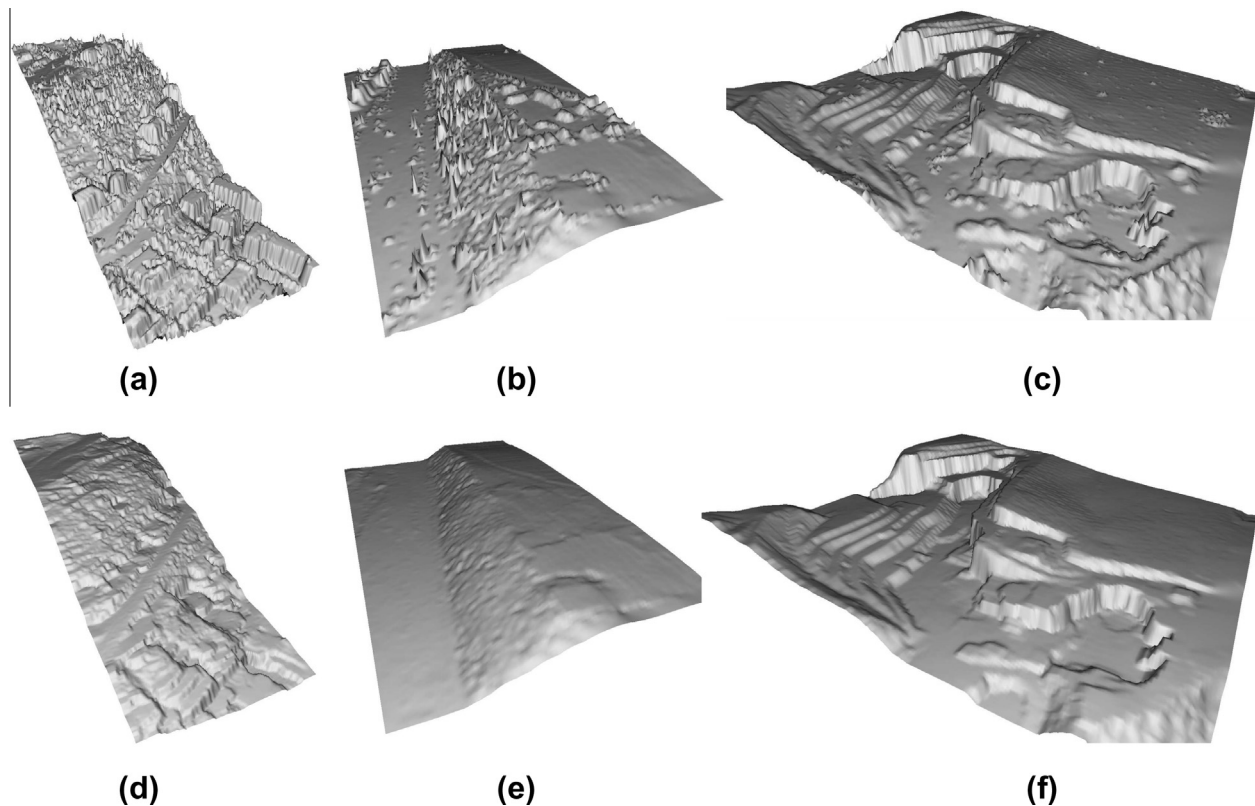


Fig. 4. Generation of DTMs from (a–c) ISPRS benchmark datasets, were (d–f) the lowest accuracy is achieved: (a and d) *samp11* contains the highest Total error, (b and e) *samp51* where the highest Total error in comparison to SMRF is introduced, and (c and f) *samp53* where the highest average Total error of DTM is obtained.

efficient in the great majority of cases in comparison with SMRF by [Pingel et al. \(2013\)](#). Approximately 7% improvement was achieved regarding the average Total error and standard deviation was reduced by approximately 20%. In fact, the SMRF algorithm performed better than the proposed method when considering the best-case scenario e.g. *samp61* from [Table 1](#), and worst when considering the worst-case scenarios e.g. *samp11* from [Table 1](#) (see [Fig. 4a](#)). In that sense, the proposed method may be considered as more stable. However, the proposed method introduced a greater average Type II error than the compared methods. As the

achieved Type II errors are comparable in most cases, test samples *samp52*, *samp53*, and *samp61* could be exposed as the main contributors to this error. In these test samples the number of non-ground points is significantly smaller than the number of ground points. Thus, a small number of misclassified non-ground points results in an unproportionally high Type II error that does not influence the Total error. Although Type II error could be suppressed using lower values of *n* and *b*, this leads to an increased Type I error that has a more significant effect on the Total error in these cases.

Table 2

Evaluation results with ISPRS reference classification in test-cases of Vaihingen, Germany, and Toronto, Canada. Average results of both-test cases are highlighted.

Test-case	Location	Per-area			Per-object			Per-object > 50 m ²		
		CP	CR	Q	CP	CR	Q	CP	CR	Q
Area1	Vaihingen	90.3	91.7	83.5	86.5	93.9	81.9	100.0	96.6	96.6
Area2	Vaihingen	89.9	97.8	88.1	78.6	91.7	73.4	100.0	100.0	100.0
Area3	Vaihingen	88.9	96.2	85.9	76.8	95.6	74.2	97.4	100.0	97.4
Average		89.7	95.2	85.8	80.6	93.7	76.5	99.1	98.9	98.0
Std. dev.		0.58	2.58	1.88	4.21	1.59	3.83	1.23	1.62	1.45
Area4	Toronto	93.7	94.9	89.2	98.3	94.9	93.4	100.0	96.6	96.6
Area5	Toronto	94.3	93.7	88.7	84.2	88.9	76.2	91.4	97.0	88.9
Average		94.0	94.3	88.9	91.2	91.9	84.8	95.7	96.8	92.8
Std. dev.		0.30	0.60	0.25	7.05	3.00	8.60	4.30	0.20	3.85

However, a greater Type II error that significantly effects the Total error could be noticed in the case of *samp51*. Both of the compared methods consequently performed considerably better in this case. This test sample contains low vegetation on a steep slope (see Fig. 4b), where a relatively large morphological gradient was measured. As morphological gradient is used in the definition of the labelling threshold function (see Eq. (9)), filtering of the lowest vegetation points was prevented. An obvious solution to this problem would be to multiply a gradient by some constant (e.g. by multiplying the morphological gradient in Eq. (9) by a constant of 0.5, the Total error was reduced by almost 1% from 2.73% to 1.83%). However, an additional user-defined parameter should be introduced for this purpose that is actually superfluous for all the other cases. This particular test case was therefore a trade-off between user-friendliness and the accuracy of the method.

Further analysis on the method's performance can be achieved by considering the *b* parameter from Table 1. Namely, the proposed method generates DTM before the labelling of LiDAR points is completed. The value of *b* therefore provides a sense of DTM's accuracy by defining the boundary where the best separation of ground from non-ground was achieved. A more exact evaluation of the accuracy could be given by measuring the average absolute height distances of ground points from DTM. In this case, the worst results were obtained on samples *samp11*, *samp41*, and *samp53* (see Fig. 4c), where 0.25 m, 0.26 m, and 0.28 m average absolute distances were obtained accordingly, whilst the overall average distance was 0.11 m. In the cases of *samp11* and *samp53*, the major contributors to this error are discontinuities on the terrain, where small (in terms of the number of points) misclassification results in a greater height difference (over 20 m). In the case of *samp41* the main reason for this error is a misclassified low outlier near the strip of missing data.

4.2. Evaluation of building-detection benchmark

The proposed method for building detection in LiDAR data was tested on all five benchmark test-areas provided by ISPRS in the Test Project on Urban Classification and 3D Building Reconstruction. The first three test-areas were located within the town of Vaihingen, Germany, characterised by older architectural styles. They included various smaller buildings that were partially obstructed by high-vegetation, and a few high-rise residential buildings. The last two test areas are located within the city of Toronto, Canada and were characterised by modern architecture with low and high-storey buildings. Many of these buildings fell into the high-rise category. The Vaihingen data set contains over 18 million points and the Toronto dataset has nearly 14 million points. Without considering the estimation of geometric attributes (also used for DTM generation), the execution times measured on Intel® Core™ i7 CPU with 8 GB of main memory were 11.6 s and 8.3 s,

respectively. Two different sets of thresholds were used in order to achieve optimal results for both LiDAR test-sets. In the test-areas from Vaihingen, the threshold values were given as $t^W = 2.0$ m, $t^H = 1.5$ m, $t^R = 5.0$ m, $t^P = 0.05$ m, and $t^A = 25$ m². On the other hand, in the test-areas from Toronto $t^H = 2.5$ m as higher buildings were contained, and $t^A = 100$ m² in order to compensate for larger areas of missing building-points. The definition of the fitting-window was in both cases given as $F = 3$, whilst the linking-window was greater in the case of Toronto than in that of Vaihingen due to larger contained obstacles. In the case of Toronto $L = 5$ was used, and in case of Vaihingen $L = 3$. The accuracy of the method was evaluated according to ISPRS reference data. For this purpose, the completeness CP[%], correctness CR[%], and quality Q[%] metrics were used, as proposed by Rutzing et al. (2009). The results of the evaluation are shown in Table 2.

In comparison with the related methods,¹ the results of the proposed method in the Vaihingen test areas were, in terms of correctness, comparable even with those methods that rely on LiDAR data fusion with aerial images (especially in the cases of areas 2 and 3) but lower in terms of completeness. However, the achieved completeness was higher than that achieved by most of the methods relying on LiDAR data alone. In the cases of the Toronto test-areas (areas 4 and 5), on the other hand, the proposed method outperformed all the tested methods. The advantages and drawbacks of the proposed method are further exposed in the continuation.

Three main reasons can be exposed for under-performing within the test-areas located in Vaihingen, where the average completeness was 89.7%. One important contributor to these errors were building details (see Fig. 5) that are often smaller than the fitting-window size used in LoFS (see Section 3.1). Although the fitting-window size might be decreased for this purpose, this leads to a considerable increase in errors regarding correctness as dense vegetation might often be recognised as a building (see Fig. 5d). Thus, a comprehensive solution to this problem can only be provided by fusing LiDAR data with aerial images. Another reason for the lower completeness was the area-opening performed during the last step of the method when removing false positives from the vegetation areas. Although a relatively low area threshold was used, several partially-detected buildings were removed. Finally, not all the building details were actually contained within the LiDAR data. As considerable portions of the buildings were missing (see Fig. 5c), the method was unable to detect them. This was, however, the main reason for all those methods relying only on LiDAR data to under-perform in comparison with the data fusion approaches. On the other hand, considerably higher completeness was achieved in the test-areas from Toronto, due to the lower number of details in comparison with the Vaihingen test-sides.

¹ See results of MAR_13 available at <http://www2.isprs.org/commissions/comm3/wg4/results.html>.

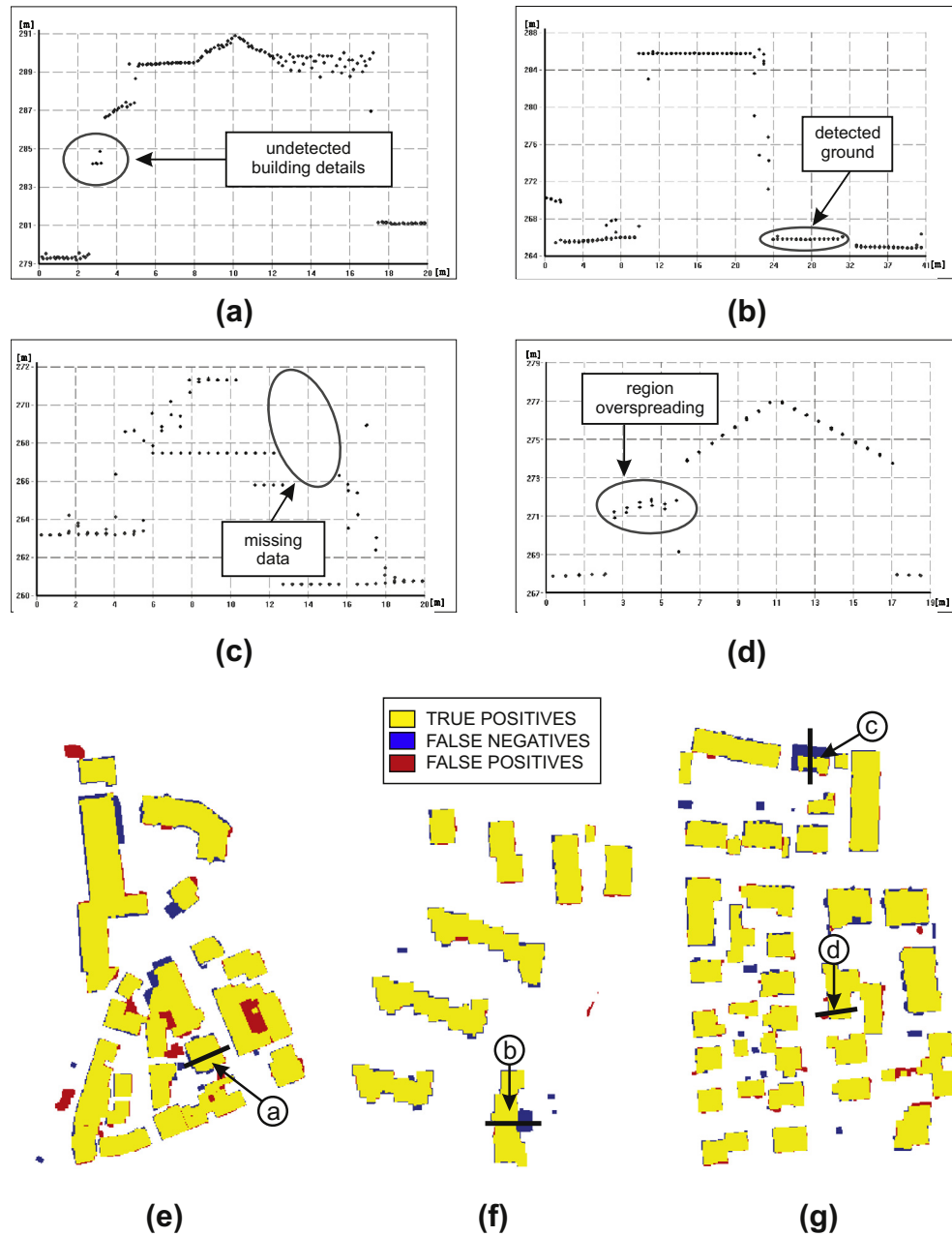


Fig. 5. Evaluation of building detection in the Vaihingen dataset where (a–d) characteristic errors are exposed and (e, f, and d) where complete evaluation results on test areas are shown.

A significant portion of errors can also be related to the errors in ground estimation. It is obvious that regions recognised as ground cannot be detected as buildings (see Fig. 5b). On the other hand some false negative ground regions might be detected as buildings (see Fig. 6c). Thus, errors in ground detection contribute to errors in completeness as well as concreteness. In terms of correctness alone, a vast majority of errors can be related to the overspreading of regions to those neighbouring trees having similar heights as the buildings. Nevertheless, this error is considerably smaller and is, in some sense, a compensation for the method being highly robust against obstacles such as trees covering the rooftops (see Fig. 6c) and points contained within a building (see Fig. 6b). This can be exposed as the key advantage of the proposed method, allowing it to achieve accurate results even under extremely difficult conditions such as the test-areas of Toronto. Although not tested by the ISPRS

benchmark test-set, this method is able to separate bridges from buildings, as seen in Appendix B.

5. Conclusion

This paper proposes new methods for ground extraction and building detection in LiDAR data by considering the geometrical, surface, and regional attributes of the contained features. Geometrical attributes, mapped from DMPs, provide a sufficient basis for ground definition, whilst additional surface and regional analysis is performed for building detection. A new algorithm for the estimation of locally fitted surfaces (LoFS) is proposed for surface analysis. By providing computationally-efficient and exact definitions of buildings' surfaces that are resistant to obstacles (e.g. trees

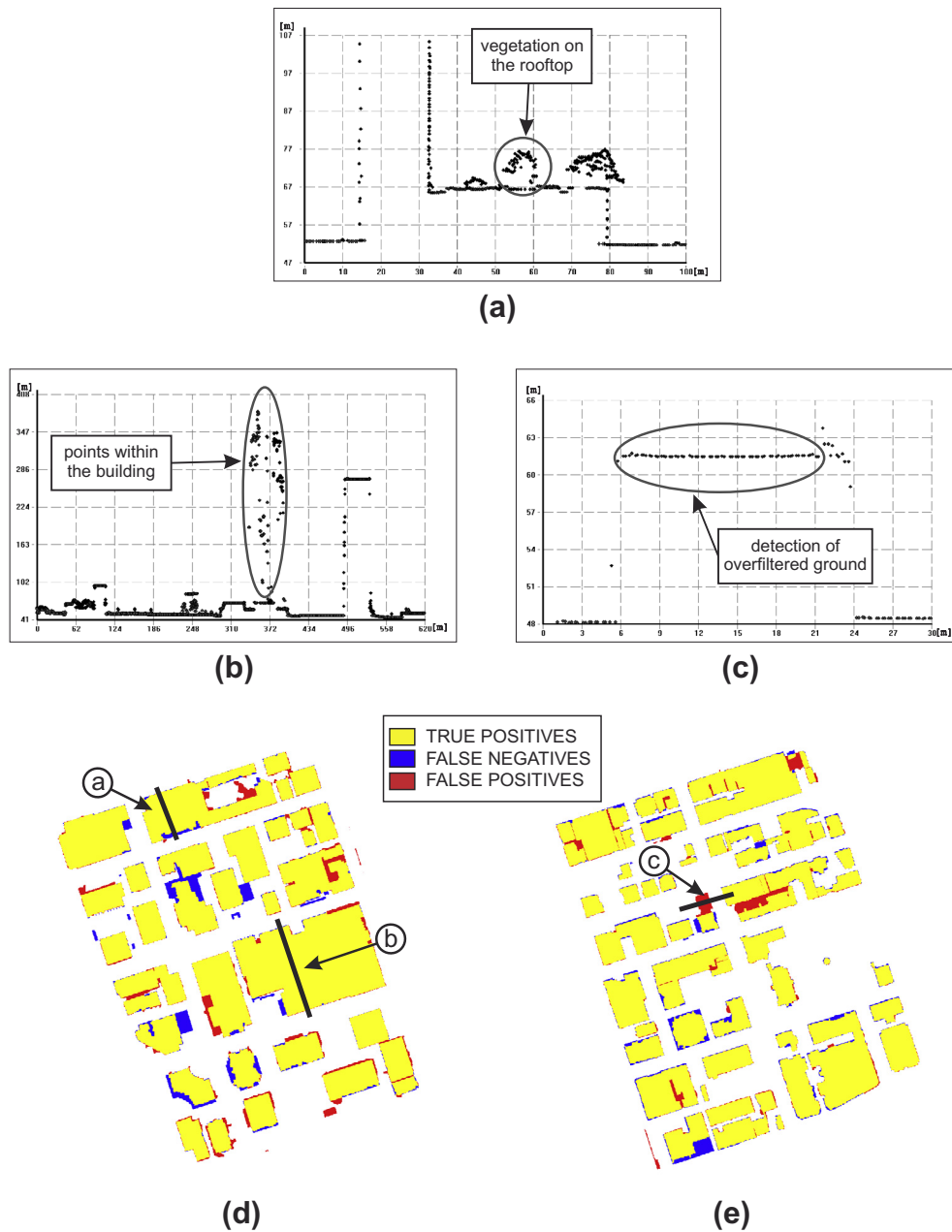


Fig. 6. Evaluation of building detection within the Toronto dataset, where (a and b) advantages and (c) characteristic errors of the proposed method are exposed and (d and e) complete evaluation results on test areas are shown.

lying over the rooftops and points within the building), LoFS has proved an important advantage of the proposed method. It also provides a foundation for regional analysis where transitions between ground and non-ground regions are observed in order to distinguish between objects such as buildings and bridges that share similar geometrical and surface properties. According to the results on the benchmark datasets provided by ISPRS,² the overspreading of building regions into neighbouring vegetation might be exposed as the main source of errors in correctness. However, the correctness of the method is comparable even to those methods that fuse aerial images with LiDAR data. On the other hand, the method produced worse results in terms of completeness in the cases of the Vaihingen datasets. Building details that are missed by

the proposed method are major contributors to these errors. On the other hand, the proposed method turns out to be well-capable of dealing with obstacles as it outperformed all the tested methods in the Toronto test-cases. In all the cases, a significant impact on the results can be related to the accuracies of the ground areas. The proposed method for ground extractions proved to be sufficient for this purpose. The evaluation of the method, achieved by ISPRS benchmark datasets for ground extraction, showed improved accuracy and reduced standard deviation of errors in comparison with the state-of-the-art approaches.

Acknowledgements

This work was supported by the Slovenian Research Agency under Grants 1000-13-0552, J2-5479, and P2-0041. This paper was produced within the framework of the operation entitled “Centre

² See results of MAR_13 available at <http://www2.isprs.org/commissions/comm3/wg4/results.html>.

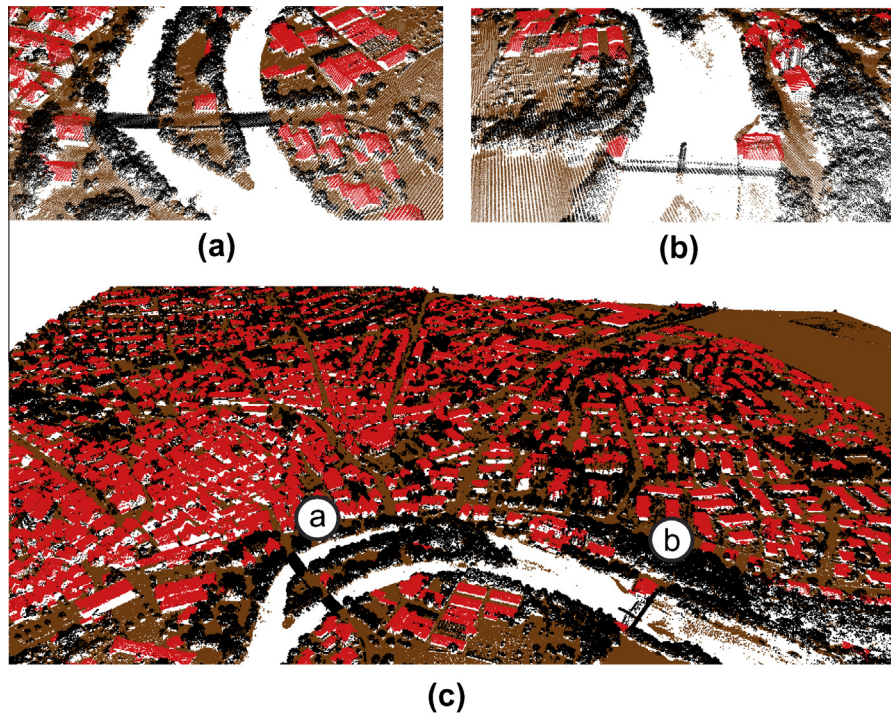


Fig. B.7. Labelled Vaihingen dataset where (a and b) buildings (red) next to bridges are successfully detected, whilst bridges are marked as unclassified (black) due to their multiple attachment to ground (brown), and (c) a panoramic view of the results.

of Open innovation and Research UM". The operation is co-funded by the European Regional Development Fund and conducted within the framework of the Operational Programme for Strengthening Regional Development Potentials for the period 2007–2013, development priority 1: "Competitiveness of companies and research excellence", priority axis 1.1: "Encouraging competitive potential of enterprises and research excellence".

Appendix A

Consider a plane given in its implicit form $\Pi(X): a_1x_1 + a_2x_2 + a_3x_3 + a_4 = 0$ and a minimisation criterion $M = \sum \Pi(X_n)^2$, where $X_n = (x_{1,n}, x_{2,n}, x_{3,n})$ and $n \in [1, N]$. It can be shown that best-fit plane passes through the average point $\bar{p} = (\frac{1}{N} \sum x_{1,n}, \frac{1}{N} \sum x_{2,n}, \frac{1}{N} \sum x_{3,n})$. Coefficients (a_1, a_2, a_3) are then defined by an eigenvector associated with the smallest eigenvalue of the matrix $A^T A$, where values $x_{1,n} - \bar{x}_1$, $x_{2,n} - \bar{x}_2$, and $x_{3,n} - \bar{x}_3$ define the first, second, and third column of A , accordingly.

Appendix B

Fig. B.7 shows that the proposed framework successfully avoids the misdetection of bridges, although it is not specifically designed for the bridge detection.

References

- Alharthy, A., Bethel, J., 2002. Heuristic filtering and 3D feature extraction from LiDAR data. *Int. Arch. Photogram. Rem. Sens. Spatial Inform. Sci.* 34 (Part 3A), 29–34.
- Bevington, P., Robinson, D.K., 2002. *Data Reduction and Error Analysis for the Physical Sciences*, third ed. McGraw-Hill, New York.
- Brovelli, M.A., Cannata, M., Longoni, U.M., 2004. LiDAR data filtering and DTM interpolation within GRASS. *Trans. GIS* 8 (2), 155–174.
- Chaplot, V., Darboux, F., Bourennane, H., Legu  dois, S., Silvera, N., Phachomphon, K., 2006. Accuracy of interpolation techniques for the derivation of digital elevation models in relation to landform types and data density. *Geomorphology* 77 (1–2), 126–141.
- Charaniya, A.P., Manduchi, R., Lodha, S.K., 2004. Supervised parametric classification of aerial LiDAR data. In: *Proceedings of the IEEE Computer Society Conference on Computer Vision and Pattern Recognition Workshop*, 27–02 June, 30. IEEE Computer Society, Washington, DC, USA.
- Chen, Q., Gong, P., Baldocchi, D., Xie, G., 2007. Filtering airborne laser scanning data with morphological methods. *Photogram. Eng. Rem. Sens.* 73 (2), 175–185.
- Chen, D., Zhang, L., Li, J., Liu, R., 2012. Urban building roof segmentation from airborne LiDAR point clouds. *Int. J. Rem. Sens.* 33 (20), 6497–6515.
- Chen, C., Li, Y., Li, W., Dai, H., 2013. A multiresolution hierarchical classification algorithm for filtering airborne LiDAR data. *ISPRS J. Photogram. Rem. Sens.* 82, 1–9, ISSN 0924-2716.
- Cheng, L., Zhao, W., Han, P., Zhang, W., Liu, Y., Li, M., 2013. Building region derivation from LiDAR data using a reversed iterative mathematic morphological algorithm. *Optics Commun.* 286, 244–250.
- Clode, S., Rottensteiner, F., Kootsookos, P., 2005. Improving city model determination by using road detection from LiDAR data. *Int. Arch. Photogram. Rem. Sens. Spatial Inform. Sci.* 36 (Part 3/W24), 159–164.
- Dietterich, T.G., 2002. Machine learning for sequential data: a review. In: *Structural, Syntactic, and Statistical Pattern Recognition*. Springer, Berlin Heidelberg, pp. 15–30.
- Dorninger, P., Pfeifer, N., 2008. A comprehensive automated 3D approach for building extraction, reconstruction, and regularization from airborne laser scanning point clouds. *Sensors* 8 (11), 7323–7343.
- Evans, B., 2008. Automated bridge detection in DEMs via LiDAR data sources for urban flood modelling. In: *Proceedings of the 11th International Conference on Urban Drainage*. Edinburgh, Scotland, 2008.
- Forlani, G., Nardinocchi, C., Scaioni, M., Zingaretti, P., 2006. Complete classification of raw LiDAR data and 3D reconstruction of buildings. *Patt. Anal. Appl.* 8 (4), 357–374.
- Haugerud, R.A., Harding, D.J., 2001. Some algorithms for virtual deforestation (VDF) of LiDAR topographic survey data. *Int. Arch. Photogram. Rem. Sens.* 34 (Part 3/W4), 211–218.
- Hermosilla, T., Ruiz, L.A., Recio, J.A., Estornell, J., 2011. Evaluation of automatic building detection approaches combining high resolution images and LiDAR data. *Rem. Sens.* 3 (6), 1188–1210.
- Kim, K., Shan, J., 2011. Building roof modeling from airborne laser scanning data based on level set approach. *ISPRS J. Photogram. Rem. Sens.* 66 (4), 484–497.
- Kraus, K., Pfeifer, N., 1998. Determination of terrain models in wooded areas with airborne laser scanner data. *ISPRS J. Photogram. Rem. Sens.* 53 (4), 193–203.
- Lee, H.S., Younan, N., 2003. DTM extraction of LiDAR returns via adaptive processing. *IEEE Trans. Geosci. Rem. Sens.* 41 (9), 2063–2069.
- Liu, X., 2008. Airborne LiDAR for DEM generation: some critical issues. *Progr. Phys. Geography* 32 (1), 31–49.

- Lohmann, P., Koch, A., Schaeffer, M., 2000. Approaches to the filtering of laser scanner data. *Int. Arch. Photogram. Rem. Sens.* 33 (Part B3/1), 540–547.
- Mallet, C., Bretar, F., Soergel, U., 2008. Analysis of full-waveform LiDAR data for classification of urban areas. *Photogrammetrie Fernerkundung Geoinformation* 5, 337–349.
- Maragos, P., 1989. Pattern spectrum and multiscale shape representation. *IEEE Trans. Patt. Anal. Mach. Intell.* 11 (7), 701–716.
- Meng, X., Wang, L., Currit, N., 2009. Morphology-based building detection from airborne LiDAR data. *Photogram. Eng. Rem. Sens.* 75 (4), 437–442.
- Mongus, D., Žalik, B., 2012. Parameter-free ground filtering of LiDAR data for automatic DTM generation. *ISPRS J. Photogram. Rem. Sens.* 67, 1–12.
- Mongus, D., Žalik, B., 2014. Computationally efficient method for the generation of a digital terrain model from airborne LiDAR data using connected operators. *IEEE J. Select. Top. Appl. Earth Observ. Rem. Sens.* 7 (1), 340–351.
- Mongus, D., Lukač, N., Obrul, D., Žalik, B., 2013. Detection of planar points for building extraction from LiDAR data based on differential morphological and attribute profiles. *ISPRS Ann. Photogram. Rem. Sens. Spatial Inform. Sci.* 2 (Part 3/W1), 21–26.
- Neidhart, H., Sester, M., 2008. Extraction of building ground plans from LiDAR data. *Int. Arch. Photogram. Rem. Sens. Spatial Inform. Sci.* 37 (Part B2), 405–410.
- Pesaresi, M., Benediktsson, J.A., 2001. A new approach for the morphological segmentation of high-resolution satellite imagery. *IEEE Trans. Geosci. Rem. Sens.* 39 (2), 309–320.
- Pfeifer, N., Reiter, T., Briesse, C., Rieger, W., 1999. Interpolation of high quality ground models from laser scanner data in forested areas. *Int. Arch. Photogram. Rem. Sens.* 32 (Part 3/W14), 31–36.
- Pingel, T.J., Clarke, K.C., McBride, W.A., 2013. An improved simple morphological filter for the terrain classification of airborne LiDAR data. *ISPRS J. Photogram. Rem. Sens.* 77, 21–30.
- Priestnall, G., Jaafar, J., Duncan, A., 2000. Extracting urban features from LiDAR digital surface models. *Comput., Environ. Urban Syst.* 24 (2), 65–78.
- Rottensteiner, F., 2003. Automatic generation of high-quality building models from LiDAR data. *IEEE Comput. Graph. Appl.* 23 (6), 42–50.
- Rottensteiner, F., Briesse, C., 2002. A new method for building extraction in urban areas from high-resolution LiDAR data. *Int. Arch. Photogram. Rem. Sens. Spatial Inform. Sci.* 34 (Part 3A), 295–301.
- Rottensteiner, F., Trinder, J., Clode, S., Kubik, K., 2007. Building detection by fusion of airborne laser scanner data and multi-spectral images: performance evaluation and sensitivity analysis. *ISPRS J. Photogram. Rem. Sens.* 62 (2), 135–149.
- Ruijin, M., 2005. DEM generation and building detection from LiDAR data. *Photogram. Eng. Rem. Sens.* 71 (7), 847–854.
- Rutzinger, M., Rottensteiner, F., Pfeifer, N., 2009. A comparison of evaluation techniques for building extraction from airborne laser scanning. *IEEE J. Select. Top. Appl. Earth Observ. Rem. Sens.* 2 (1), 11–20.
- Salah, M., Trinder, J., Shaker, A., 2009. Evaluation of the self-organizing map classifier for building detection from LiDAR data and multispectral aerial images. *J. Spatial Sci.* 54 (2), 15–34.
- Salembier, P., Wilkinson, M.H., 2009. Connected operators: a review of region-based morphological image processing techniques. *IEEE Signal Process. Magaz.* 136 (6), 136–157.
- Sampath, A., Shan, J., 2010. Segmentation and reconstruction of polyhedral building roofs from aerial LiDAR point clouds. *IEEE Trans. Geosci. Rem. Sens.* 48 (3), 1554–1567.
- Shan, J., Sampath, A., 2005. Urban DEM generation from raw LiDAR data: a labeling algorithm and its performance. *Photogram. Eng. Rem. Sens.* 71 (2), 217–226.
- Sithole, G., 2001. Filtering of laser altimetry data using a slope adaptive filter. *Int. Arch. Photogram. Rem. Sensing* 34 (Part 3/W4), 203–210.
- Sithole, G., Vosselman, G., 2004. Experimental comparison of filter algorithms for bare earth extraction from airborne laser scanning point clouds. *ISPRS J. Photogram. Rem. Sens.* 59 (1–2), 85–101.
- Tarsha-Kurdi, F., Landes, T., Grussenmeyer, P., 2007. Hough-transform and extended RANSAC algorithms for automatic detection of 3D building roof planes from lidar data. *Int. Arch. Photogram. Rem. Sens. Spatial Inform. Syst.* 36 (Part 3/W52), 407–412.
- Verma, V., Kumar, R., Hsu, S., 2006. 3D building detection and modeling from aerial LiDAR data. In: *Proceedings of the IEEE Computer Society Conference on Computer Vision and Pattern Recognition*, 17–22 June, vol. 2, IEEE Computer Society, Washington, DC, USA, pp. 2213–2220.
- Vosselman, G., 2000. Slope based filtering of laser altimetry data. *Int. Arch. Photogram. Rem. Sens.* 33 (Part B3/2), 935–942.
- Vu, T.T., Yamazaki, F., Matsuoka, M., 2009. Multi-scale solution for building extraction from LiDAR and image data. *Int. J. Appl. Earth Observ. Geoinform.* 11 (4), 281–289.
- Wang, C.K., Tseng, Y.H., 2010. DEM generation from airborne LiDAR data by an adaptive dualdirectional slope filter. *Int. Arch. Photogram. Rem. Sens. Spatial Inform. Sci.* 38 (Part 7B), 628–632.
- Wang, O., Lodha, S.K., Helmbold, D.P., 2006. A Bayesian approach to building footprint extraction from aerial LiDAR data. In: *Proceedings of the Third International Symposium on 3D Data Processing, Visualization, and Transmission*. IEEE Computer Society, Chapel Hill, NC, USA, pp. 192–199.
- You, S., Hu, J., Neumann, U., Fox, P., 2003. Urban site modeling from LiDAR. In: Kumar, V., Gavrilova, M., Tan, C., Lecuyer, P. (Eds.), *Computational Science and its Applications ICCSA 2003, Lecture Notes in Computer Science*, vol. 2669. Springer, Berlin Heidelberg, pp. 579–588.
- Zhang, K., Whitman, D., 2005. Comparison of three algorithms for filtering airborne LiDAR data. *Photogram. Eng. Rem. Sens.* 71 (3), 313–324.
- Zhang, K., Chen, S.C., Whitman, D., Shyu, M.L., Yan, J., Zhang, C., 2003. A progressive morphological filter for removing nonground measurements from airborne LiDAR data. *IEEE Trans. Geosci. Rem. Sens.* 41 (4), 872–882.
- Zhang, K., Yan, J., Chen, S.C., 2006. Automatic construction of building footprints from airborne LiDAR data. *IEEE Trans. Geosci. Rem. Sens.* 44 (9), 2523–2533.
- Zhou, G., Song, C., Simmers, J., Cheng, P., 2004. Urban 3D GIS from LiDAR and digital aerial images. *Comput. Geosci.* 30 (4), 345–353.